

Surface activity of rapidly rotating stars from simultaneous X-ray and UV observations with *AstroSat*

Lalitha Sairam^{1,*}, Utkarsh Pathak^{2,3} and Kulinder Pal Singh^{3,4}

¹School of Physics & Astronomy, University of Birmingham, Edgbaston, Birmingham B15 2TT, UK.

²Indian Institute of Technology Bombay, Powai, Mumbai-400076, India.

³Department of Physical Sciences, Indian Institute of Science Education and Research Mohali, Sector 81, SAS Nagar, Manauli PO 140306, India.

⁴Tata Institute of Fundamental Research, Homi Bhabha Road, Mumbai 400005, India.

*Corresponding author. E-mail: L.Sairam@bham.ac.uk

MS received July 2023; accepted

Abstract.

Our study focuses on analysing the coronal, transition and chromospheric activity of four rapidly rotating stars located within 50 pc in the solar neighbourhood. We have used the multi-wavelength capabilities of *AstroSat*, to investigate the outer atmospheres of AB Dor, BO Mic, DG CVn and GJ 3331. These stars, classified as M and K type active stars, are known for their short rotation periods, leading to increased surface magnetic activity. Our soft X-ray observations provide the coronal properties such as emission measures, temperatures and elemental coronal abundances. We report the detection of X-ray flares from AB Dor, BO Mic, and DG CVn, while UV light curves reveal flares in both BO Mic and DG CVn.

Keywords. stellar activity — coronae — chromosphere — flares; Stars: AB Dor, Bo Mic, DG CVn, GJ3331

1. Introduction

Low-mass stars possess stratified atmospheres consisting of the photosphere, chromosphere, transition region and corona. Each of these atmospheric layers has a characteristic temperature and features associated with magnetic activity (Kochukhov, 2021; Hindman & Jain, 2022). In general, the Sun is considered to be a prototype of a low mass main-sequence star, and we often extrapolate the solar atmospheric knowledge to other stars. The first evidence of solar magnetic activity was provided by the presence of photospheric spots also known as sunspots (Clark & Stephenson 1978, Wittmann & Xu 1987, Usoskin 2017, and references therein). The observations of sunspots were later complemented by the observations in multiple wavelength bands such as ultraviolet, X-ray and radio wavebands tracing different solar atmospheric layers and their associated activity phenomena (Hathaway, 2015). Additionally the different layers of atmosphere may not be physically disconnected, for instance, during a flare the material from the chromospheric layer is transported to the corona causing the coronal density and metallicity to change temporarily (Sylwester et al. 1984). However, several studies of low-mass stars have shown that such spatial correlations between the different layers of

the atmosphere and their associated magnetic activity phenomenon may or may not be similar to that of the Sun. The heating mechanism of the outer layers of the atmosphere both in the stars and the Sun still remains a puzzle (Toriumi & Airapetian, 2022).

The hot coronal X-ray emission of low mass stars arises from the magnetically confined plasma with temperatures higher than 10^6 K (Güdel 2004). Systematic studies of low mass stars in X-rays shows that many of these stars are considerably more active than the Sun and also far more rapidly rotating (Pallavicini et al. 1981). Stars with short rotation periods exhibit activity-related features such as spots, flares, enormous emission in activity sensitive chromospheric lines (Ca II and H α), X-rays and ultraviolet wavelengths. In comparison to the Sun with $\frac{L_{X,Sun}}{L_{bol,Sun}} \sim 10^{-6}$ rapid rotators are known to possess a so called saturated corona with the $\frac{L_X}{L_{bol}} \sim 10^{-3}$ (García-Alvarez et al., 2008; Lalitha et al., 2017). This raises a concern in what respect do the rapid rotators differ from the Sun to accommodate the excess X-ray emission from their coronae.

Our current knowledge of the coronae and outer atmospheres of rapid rotators are mostly based on individual measurements in either X-rays or UV. The UV emission is mostly observed in the transition region whereas X-ray emissions are associated with the coro-

Table 1. Properties of stars observed with *AstroSat*

	AB Dor	BO Mic	DG CVn	GJ 3331
Spectral type	K0V	K3V	M4Ve	M1.5
V (mag)	7.0	9.34	12.02	10.41
Distance* (pc)	14.85 ± 0.10	51.02 ± 1.50	18.29 ± 0.11	19.83 ± 0.01
P_{rot} (d)	0.514	0.380	0.2683	0.34/9.8
$v \sin i$ (km s ⁻¹)	91 ± 1	134 ± 10	55.5	5.2
R_{\star} [R_{\odot}]	0.96 ± 0.06	1.06 ± 0.04	0.46	0.80 ± 0.05

Note: Distances are based on parallax measurements in Gaia EDR3 (Gaia Collaboration et al., 2016, 2021). DG CVn distance is calculated from parallax measurement in Gaia DR2 (Gaia Collaboration et al., 2016, 2018). Radius are based on Drake et al. (2015), Dunstone et al. (2006), Osten et al. (2016), and Messina et al. (2014).

nal region, leading to an invariable connection between the two regions during enhanced activities. While the near-ultraviolet (NUV) band is dominated by the chromospheric emission line the far-ultraviolet (FUV) comprises emission lines from the transition region. Stelzer et al. (2013) investigate the dependence of the UV excess on the X-ray flux using existing archival data. They found a strong correlation between coronal activity and emission in the transition region. To unravel this connection, we are carrying out a systematic survey of fast rotators simultaneously with the Ultra Violet Imaging Telescope and the Soft X-ray Telescope instruments onboard *AstroSat*. We used Cutispoto et al. (2002) to identify fast rotators in the solar-neighbourhood. In this study we focus on four stars: AB Dor, BO Mic, DG CVn, and GJ 3331. These stars share common traits of high magnetic activity, including high rotational velocities, and enhanced chromospheric and coronal emissions. The primary difference lies in their spectral classification, with AB Dor and BO Mic classified as K dwarfs, while DG CVn and GJ 3331 are classified as M dwarfs. We provide a detailed description of each star and their known properties are given below. The fundamental stellar properties of all our targets are given in Table 1.

1. AB Dor: A young active K dwarf star (~ 40 – 50 Myr, Guirado et al. 2011), is a member of the eponymous moving group AB Doradus Moving Group, associated with a group of 30 stars. It is an ultrafast rotator with a rotational speed $v \sin i = 91 \pm 1$ km s⁻¹ (Collier Cameron & Donati, 2002) and a rotation period = 0.514 days (Kürster, 1994). It has shown a high level of magnetic activity with an average $\frac{L_X}{L_{\text{bol}}} \sim 10^{-3}$. It is a quadruple system of a pair of binary stars AB Dor A, AB Dor B, $9.5''$ away. AB Dor B is 60 times bolometrically fainter than AB Dor A. It is a binary system of AB Dor Ba, AB Dor Bb with $0.7''$ separation first observed with Aus-

tralian Telescope Compact Array at radio wavelengths (Azulay et al., 2015). AB Dor C is the close companion of AB Dor A, with $0.16''$ separation.

2. BO Mic: An active K3V(e) star present in the constellation Microscopium, about 51.02 ± 1.5 parsecs away (Gaia Collaboration et al., 2016, 2021). It was first reported in the all-sky EUV ROSAT mission, with the largest stellar flare. It has a radial velocity of -6.5 ± 2.0 km s⁻¹ with an estimated $v \sin i$ of 134 ± 10 km s⁻¹ (Wolter et al., 2005); it is also known as Speedy Mic for its fast rotation (Bromage et al., 1992) with a rotation period of 0.380 ± 0.004 days (Cutispoto et al., 1997). It is possibly a young pre-main-sequence star with high lithium abundance, strong photometric, and chromospheric activity (Anders et al., 1993). It has been observed to have an average X-ray flux of 3.7×10^{-12} ergs cm⁻² s⁻¹ (Singh et al., 1999). Its differential rotation is weaker than the Sun, with its spot pattern changing nearly every 2.5 stellar rotations (Wolter et al., 2005).

AB Dor and BO Mic are two prototypical active ultra-fast rotators which have been previously studied by us at X-ray wavelengths (Wolter et al., 2008; Lalitha et al., 2013; Lalitha & Schmitt, 2013). Both the stars show moderate flares in X-rays and/or UV in nearly every stellar rotation as well as occasional large flares.

3. DG CVn (GJ 3789): A binary system in which one of the components is a rapidly rotating M-type dwarf. DG CVn is listed in the Washington Double Star Catalog as a binary of M dwarfs with separation $\sim 0.2''$ located at a distance of 18.29 ± 0.11 parsecs (Gaia Collaboration et al., 2016, 2018), with an estimated age of only 30 Myr. The system has fast rotation with $v \sin i \sim 55.5$ km s⁻¹

Table 2. Log of *AstroSat* SXT and UVIT observations

Star Name	Instrument	Observation ID	Start Time (UT) Y:M:D:H:M:S	Stop Time (UT) Y:M:D:H:M:S	Effective Exposure (s)	Mean Count Rate	Energy band
AB Dor	SXT	9000000274	2016:01:15:11:57:43	2016:01:16:04:46:40	17346	1.075±0.009	0.3-6.0 keV
AB Dor	SXT	9000000306	2016:01:31:11:13:32	2016:02:01:05:11:32	17272	1.132±0.009	0.3-6.0 keV
BO Mic	SXT	9000002104	2018:05:17:21:24:36	2018:05:20:12:34:13	41862	0.173±0.003	0.3-6.0 keV
	UVIT FUV (F148W)	9000002104	2018:05:17:22:42:12	2018:05:19:18:48:02	17138	0.872±0.134	1231-1731 Å
DG CVn	SXT	9000001218	2017:05:11:07:47:57	2017:05:12:03:33:19	21687	0.065±0.002	0.3-6.0 keV
	UVIT NUV (N242W)	9000001218	2017:05:11:09:39:19	2017:05:12:03:10:48	81	9.391±3.121	2026-2811 Å
	UVIT FUV (F148W)	9000001218	2017:05:11:09:39:14	2017:05:12:03:10:44	1102	0.396±0.164	1231-1731 Å
GJ 3331	SXT	9000000898	2016:12:18:13:56:41	2016:12:19:06:36:30	14748	0.200±0.004	0.3-6.0 keV
	UVIT NUV (N279N)	9000000898	2016:12:18:13:58:45	2016:12:19:09:59:29	15760	2.398±0.401	2747-2837 Å
	UVIT FUV F148W (F148W)	9000000898	2016:12:18:13:58:49	2016:12:19:09:59:25	11749	0.316±0.124	1231-1731 Å

and rotation period $P_{\text{rot}} \sim 0.28\text{d}$ (Delfosse et al., 1998; Mohanty & Basri, 2003). DG CVn was detected in the ROSAT All-Sky Survey Bright Source Catalog with $L_X \sim 2.0 \times 10^{28} \text{ ergs s}^{-1}$ and $\frac{L_X}{L_{\text{bol}}} \sim -3.22$ Voges et al. 1999. It is also a radio-emitting source (Helfand et al., 1999). On 2014 April 23, Drake et al. (2014) reported a hard X-ray superflare on DG CVn, detected with the Burst Alert Telescope (BAT) onboard the *Swift* satellite, with a peak 15-50 keV flux of $\sim 300 \text{ mCrab}$ (Osten et al., 2016). This flare was bright enough to trigger *Swift* and cause it to slew automatically to the source. This stellar super-flare is one of only a handful of stars that have been bright enough to trigger *Swift* in such a fashion, and the previous ones (Osten et al., 2007, 2010) have revealed the extreme end of magnetic reconnection in normal non-degenerate stars.

- GJ 3331: A multiple stellar system, BD 211074, is reported in the Washington Catalog of Visual Double Stars as a stellar system consisting of three visual M-type stars (Mason et al., 2001). The primary component, GJ 3331, is an M1.5 star with $V = 10.41 \text{ mag}$, the secondary component, GJ 3332, an M2.5 star with $V = 11.67 \text{ mag}$ and the tertiary component, BD 211074C with a M5 or later spectral type (Jao et al., 2003). Our target of interest, GJ 3331, is a very rapidly rotating ($P_{\text{rot}} \sim 0.34\text{d}$, Kiraga & Stepień 2007). However, Messina et al. (2014) found a $P_{\text{rot}} \sim 9.3\text{d}$ consistent with $v \sin i \sim 5.3 \text{ km s}^{-1}$ (Reiners et al., 2012; Malo et al., 2014). It was detected in the extreme ultraviolet (EUV) by the ROSAT Wide Field Camera (WFC) and listed in the WFC Bright Source Catalogue as RE 0506-213 (Pounds et al., 1993). GJ 3331 is

an active stars with a strong X-ray emission detected by ROSAT ($L_X \sim 1.4 \times 10^{29} \text{ ergs s}^{-1}$ and $\frac{L_X}{L_{\text{bol}}} \sim -3.01$, Voges et al. 1999). Both components, A and the unresolved BC, are listed in the catalog of UV Ceti-type flare stars compiled by Gershberg et al. (1999).

This paper is organised as follow: in §2 we describe the *AstroSat* observation in both X-rays and UV wavelengths and the data reduction. In §3, we present our data analysis and results from the temporal and spectral analysis. A detailed discussion for each of the target stars and our conclusion is presented in §4.

2. Observation and data reduction

The targets were observed with *AstroSat* (Singh et al., 2014). *AstroSat* is a multi-wavelength astronomy mission carrying five multi-band payloads. The stars listed here were observed with the SXT covering the 0.3-6.0 keV energy band (Singh et al., 2016, 2017), and the Ultra-Violet Imaging Telescope (Tandon et al., 2017; Tandon et al., 2020). The UVIT consists of two 35cm Ritchey-Chrétien telescopes, one covering the FUV (1250 – 1830 Å) band and the other telescope uses a dichroic beam splitter that splits the beam into the NUV (1900 – 3040 Å) and the visible (VIS: 3040 – 5500 Å) channels. Each waveband has a choice of filters as given in (Tandon et al., 2017), and have $\sim 1.8''$ resolution. The CMOS imagers used for all the bands have 512×512 pixels, with each pixel mapped to 8×8 sub-pixels, giving a pixel scale of 0.416 arc-seconds/sub-pixel (Tandon et al., 2020). A detailed description of the observations is given in Table 2.

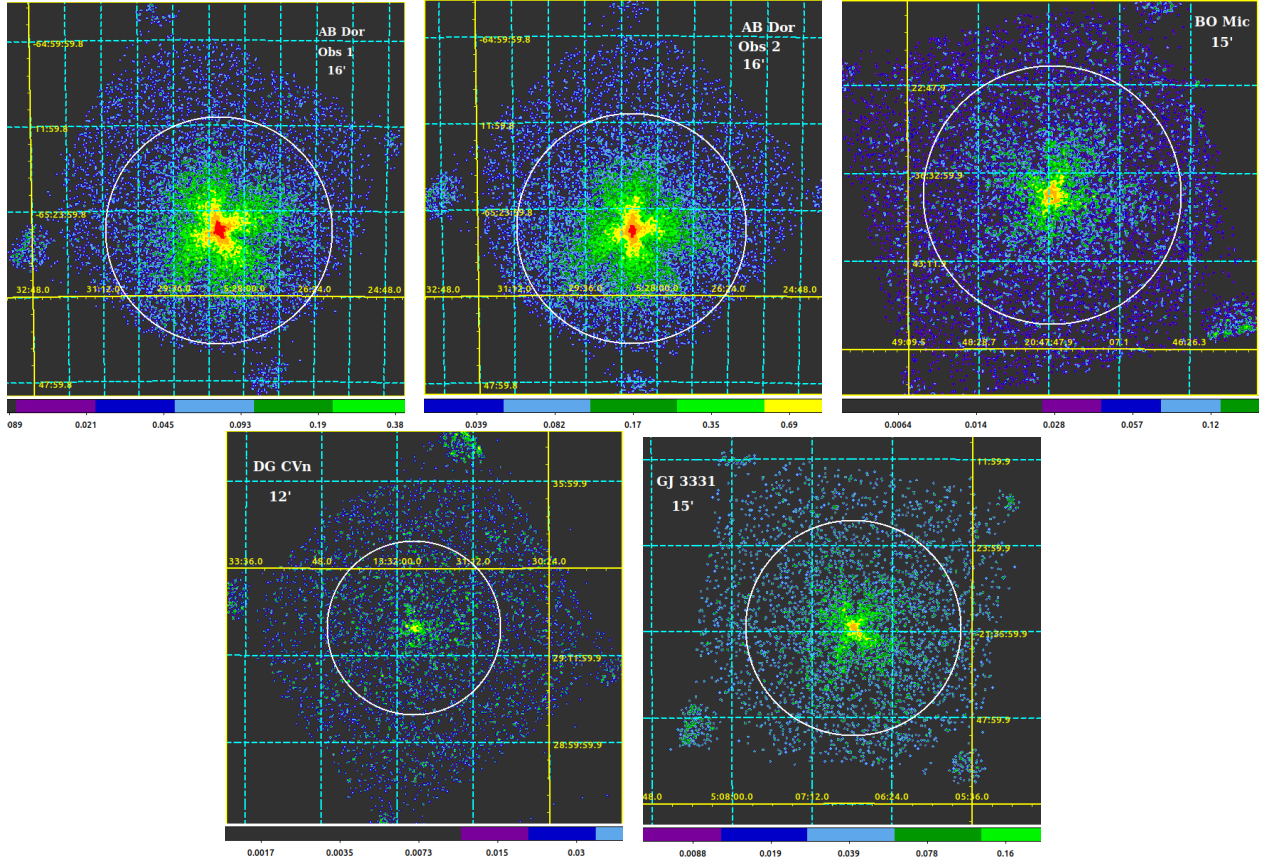


Figure 1. X-ray images of the stars in 0.3-3.0 keV energy band observed with the *AstroSat* SXT (Clockwise from top left: AB Dor (1st epoch), AB Dor (2nd epoch), BO Mic, DG CVn and GJ 3331). The white circle shows the extraction region for the light curves and spectra and the image has been smoothed with a Gaussian function of 3-pixel radius.

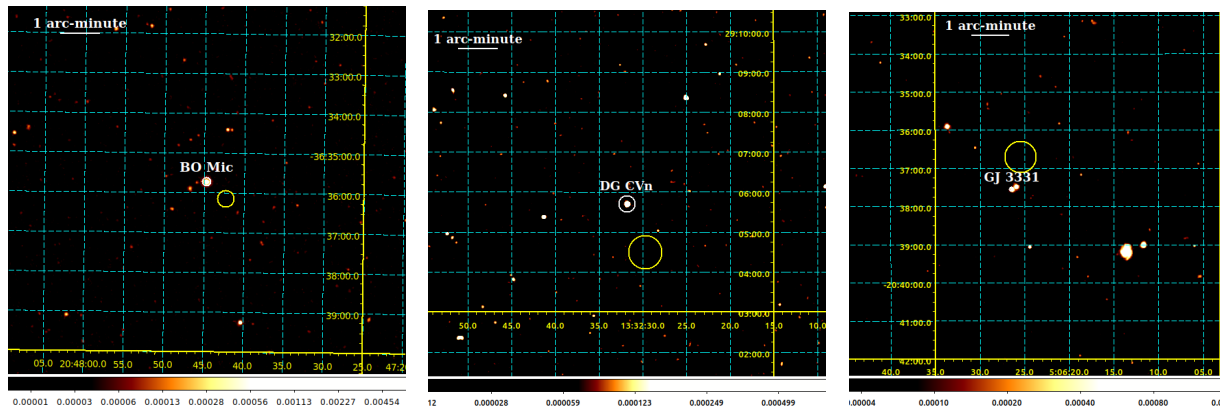


Figure 2. FUV images for each observation with the *AstroSat* UVIT (BO Mic F148W, DG CVn F148W, GJ 3331 F148W, respectively). The white circle shows the extraction region for the light curves and the yellow circle shows the background region. The images have been smoothed with a Gaussian function of 5-pixel radius, while the DG CVn F148W image from orbit 3 has been smoothed with a Gaussian function of 11-pixel radius due to the absence of combined orbits image.

2.1 Soft X-ray Telescope (SXT)

X-ray data from individual orbits (level 1 data) were reduced with the standard pipeline for the SXT using SXTPIPELINE software at the Payload Operation Centre (POC) where events are selected with event grading similar to *Swift*-XRT, see Romano et al. (2005) and events with grades > 12 are removed. All events above a preset threshold above the electronic noise level were time-tagged, applied with the coordinate transformation from the detector to sky coordinates, and bias subtracted. The bad pixels tagging, search and removal of hot and flickering pixels, and conversion from the event pulse height to the X-ray energy of the event were carried out in the pipeline. The selected events are screened for bright Earth avoidance angle of ≥ 110 degrees and those detected during the passage through the South Atlantic Anomaly (SAA) were removed using the information obtained from the Charged Particle Monitor (CPM) ensuring that the CPM rate is below 12 counts s^{-1} . Good Time Intervals (GTI) were thus generated and applied, producing level 2 data events files. A merged events file of all such cleaned events from GTIs was generated using a Julia script provided by the SXT POC team. Any residual contamination from non-X-ray events was further removed by examining the light curves for flares or dips in the energy range of 7 - 10 keV or by looking at simultaneously observed background regions if available. The useful exposure times from merged cleaned events files are listed in Table 2 for each observation.

X-ray images are made for the cleaned events in the energy range of 0.3 - 3.0 keV for AB Dor Obs 1 (id:274), AB Dor Obs 2 (id:306), BO Mic, DG CVn and GJ 3331. The images produced have been smoothed by a Gaussian with a kernel of 3 pixels (1 pixel = 4'') radius. Source counts for light curves and spectra were extracted from a circular region shown by white circles in Figure 1. The extraction radius for AB Dor Obs 1 & 2 was 16', whereas for BO Mic & GJ 3331 it was 15', and 12' for DG CVn. The extraction radius was decided after examining the radial profile of surface brightness using 25 annuli from 0.5' to 19' and making sure that $\geq 95\%$ of all the source counts were selected considering the large point spread function (PSF) of the SXT (Singh et al., 2017). The background was obtained from an annular region of 13-18' for DG CVn, while the background for other sources was taken from other observations of a deep sky region provided by the SXT POC.

The X-ray counts in the spectra of sources extracted were grouped using the *grppha* tool to ensure a minimum of 30 counts per bin. The background spectra were extracted using annuli from 13' to 18' for weaker sources like DG CVn and a deep-sky background file has been used for the rest of the observations. The

response matrix (sxt_pc_mat_g0to12.rmf) and standard ARF files (sxt_arf_excl00_v04_20190608.arf) used are available at the SXT POC website ¹.

2.2 Ultra Violet Imaging Telescope (UVIT)

The UVIT data were analysed using the Level 2 photon lists and images obtained from the ISSDC. The images were compared with Galaxy Evolution Explorer (GALEX) all-sky imaging survey (AIS) images for FUV and NUV respectively. The target stars were identified by matching stellar patterns in SAOImage DS9, and the astrometric corrections were done by translating and rotating the coordinates through *astropy* version 4.0.1. The astrometric calibrations were also verified with the SIMBAD catalog. The astrometric error achieved for BO Mic F148W (1231 - 1731 Å) field is 3'' (Figure 2,3), DG CVn F148W is 4'', DG CVn N242W (2026 - 2811 Å) is 5'' (Figure 2,3), GJ 3331 F148W is 2'', and GJ 3331 N279N (2747 - 2837 Å) is 2'' (Figure 3) from the SIMBAD catalog.

The light curves extraction was done using the photon list file for each orbit through the *curvit* python package (Joseph et al., 2021). The target star for each orbit is found by matching stellar patterns and by transforming astronomical coordinates to instrumental coordinates. The FUV PSF pedestal sets the minimum source radius for extraction, i.e., 3.33'' (Tandon et al., 2017), whereas the maximum source radius is 39.52'' (Tandon et al., 2020). The source radius was chosen based on count rate values variation on changing source radii while ensuring no other event contributes to the count rate values. The background radius was twice the source radius in most cases. The background region was kept within one arc-minute of the source with no event inside it. The time bin width was chosen based on the exposure time for that observation. Different time bin widths were compared to achieve a sufficient number of data points with small errors for each data point. The details for each extraction are as follows:

- BO Mic has a 12.5'' source radius, 25.0'' background radius, and a 50s wide time bin. A flare is observed near the end of the observation in the UVIT-F148W light curve.
- DG CVn has a 12.5'' source radius, a 25.0'' background radius, and a 15 seconds wide time bin for both F148W & N242W filters.
- GJ 3331 has a smaller radius 3.33'' for extracting the source events due to the proximity of a secondary member GJ 3332, a 25.0'' background

¹http://www.tifr.res.in/~astrosat_sxt/index.html

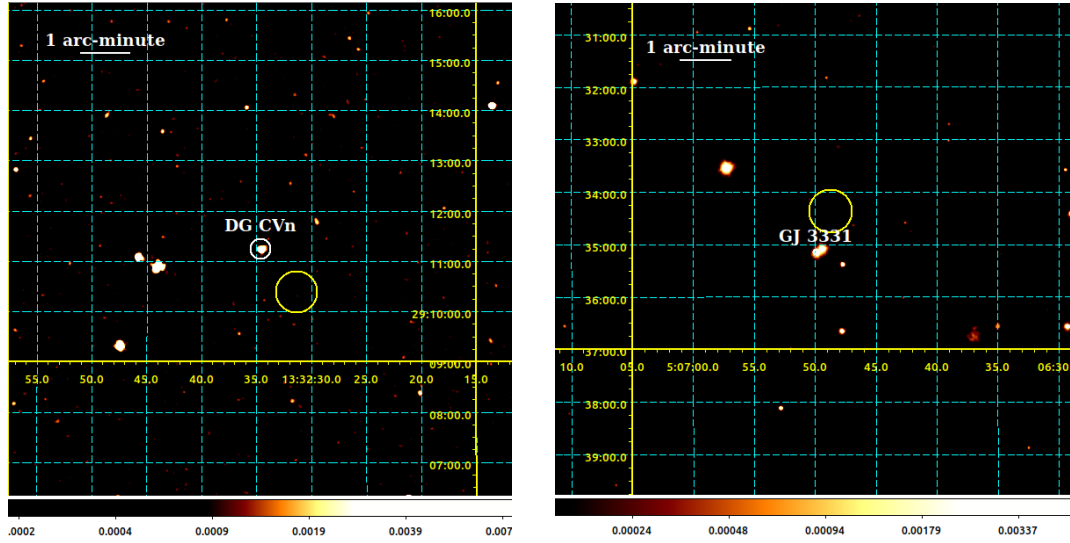


Figure 3. NUV images for each observation with the *AstroSat* UVIT (GJ 3331 N279N, and DG CVn N242W). The white circle shows the extraction region for the light curves and the yellow circle shows the background region. The images have been smoothed with a Gaussian function of 5 pixel radius, while DG CVn F148W image from orbit 3 has been smoothed with a Gaussian function of 11 pixel radius due to absence of combined orbits image.

radius, and a 20s wide time bin for F148W data, and 15s wide time bin for N279N data.

3. Data analysis and results

3.1 X-ray Temporal analysis

The X-ray light curves for our four targets were made in three energy bands - soft, hard and total for all the sources. The total energy band used is 0.3-6.0 keV, whereas the soft and hard energy bands were guided by the spectral analysis that follows to have some physical meaning relative to the spectral components identified therein and due to the presence of significant flaring episodes in some of them.

The X-ray light curves for our four targets were made in three energy bands - soft, hard and total for all the sources. The total energy band used is 0.3-6.0 keV, whereas the soft and hard energy bands were influenced by the subsequent spectral analysis. These choices were made to ensure that these energy bands have a meaningful connection to the spectral components identified in the analysis. Furthermore, the decision was influenced by the presence of significant flaring episodes observed in some of the sources. By focusing on these specific energy bands, we aim to gain insights into the physical mechanisms behind the X-ray emissions, enabling us to better understand the behaviours and characteristics of the sources. These bands and the corresponding figures shown here are:

- AB Dor: 0.3-2.0 keV for soft X-ray band and 2.0-6.0 keV for hard X-ray band.
- BO Mic: 0.3-1.2 keV for soft X-ray band and 1.2-6.0 keV for hard X-ray band.
- DG CVn: 0.3-1.0 keV for soft X-ray band and 1.0-6.0 keV for hard X-ray band.
- GJ 3331: 0.3-2.0 keV for soft X-ray band and 2.0-6.0 keV for hard X-ray band.

In Figure 4 (top panel), we plot the background-subtracted SXT light curves for AB Dor, BO Mic, DG CVn and GJ 3331. In Figure 4 (bottom panels), the hardness ratios (HR) derived from the ratio of counts in the hard band divided by the counts in the soft are plotted for each of our target. Three of our targets AB Dor, BO Mic and DG CVn show several flaring events represented by green vertical blocks in Fig.4.

During the observations several flare-like events were detected in our targets. AB Dor exhibited a flare-like event approximately 25 ks into the observations during Epoch 2. The count rate in the SXT light curves in the 0.3-6.0 keV range increased from a quiescent value of approximately 0.9 cts s^{-1} to 1.6 cts s^{-1} .

BO Mic showed two flare-like events. The first event occurred at approximately 145ks ($\sim \text{JD-2458257.55}$) into the observations, with the quiescent flux increasing from 0.25 cts s^{-1} to 1.05 cts s^{-1} . The second event occurred at approximately 180 ks ($\sim \text{JD-}$

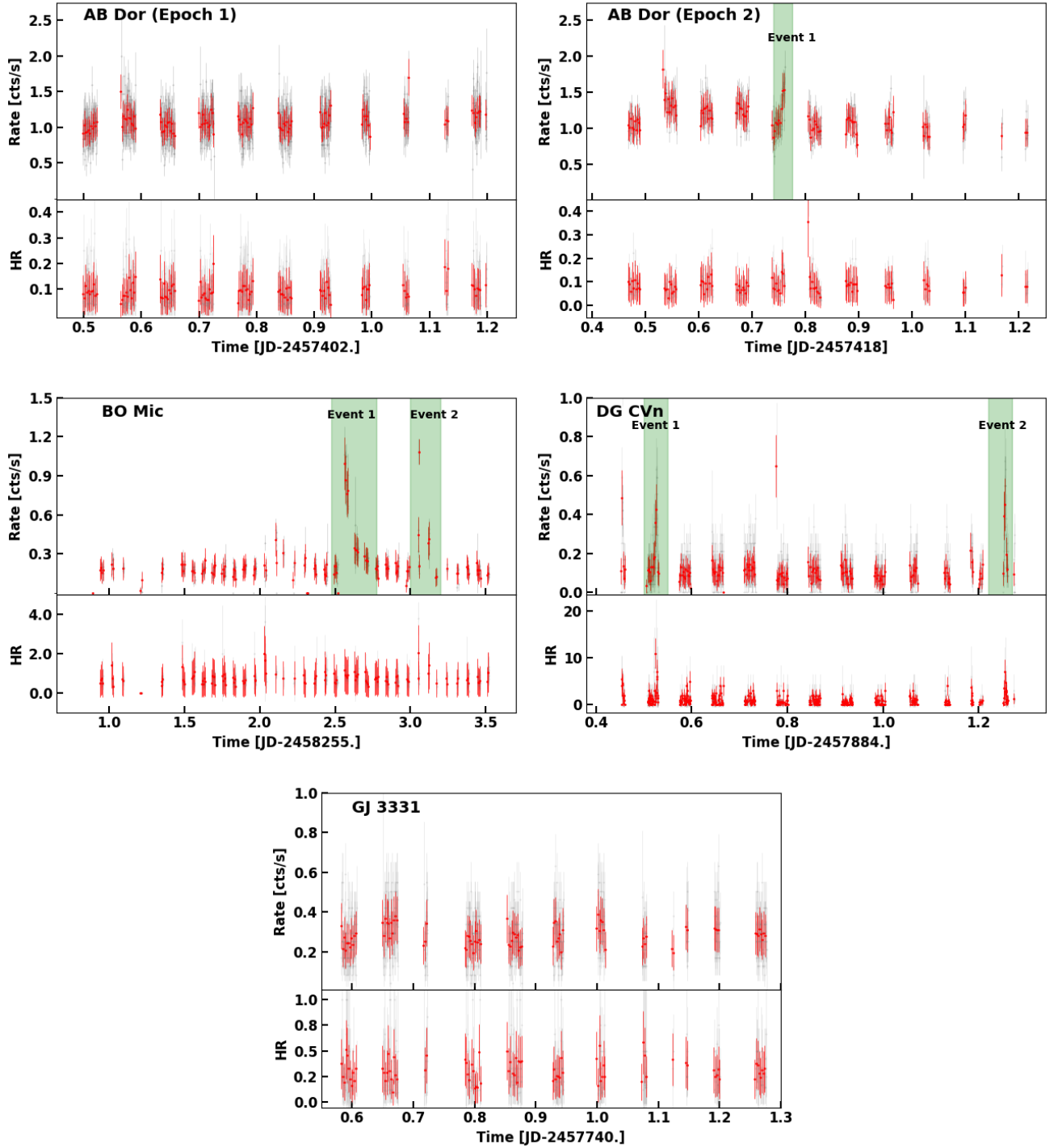


Figure 4. X-ray light curves and their corresponding hardness ratios are plotted for each of the targets. Over-plotted in red is the moving averages for better visualisation of the associated variability. The time segments corresponding to the flare-like events are represented by the vertical green blocks.

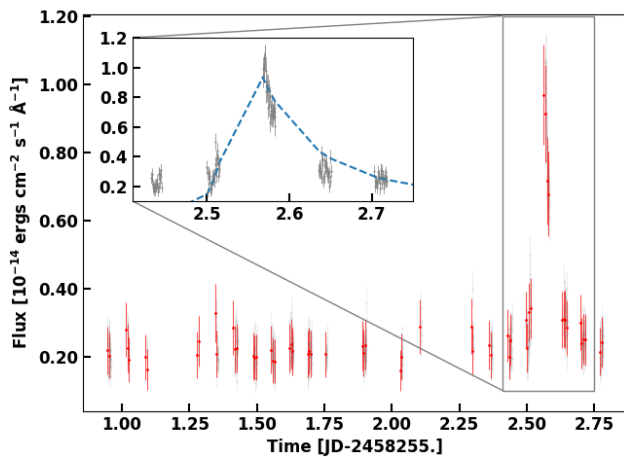


Figure 5. Combined orbits FUV light curve for BO Mic binned to 50s.

2458258.1), with the quiescent flux increasing to 1.2 cts s^{-1} .

Similarly, DG CVn displayed multiple flare-like events. The first event occurred at approximately 7ks (JD-2457884.55) into the observations, with the count rate increasing from 0.12 cts s^{-1} to 0.55 cts s^{-1} . Additionally, event 2 occurred at JD-2457885.22 showing similar changes in count rate as event 1. In Figure 4 for DG CVn, we note heating related trends in the HR. However, due to limitations in the SNR, conducting a detailed spectral analysis for these heating events observed in DG CVn may not be feasible at this time.

On the other hand, no significant flaring episodes were detected in GJ 3331 and during the first epoch observations of AB Dor. Furthermore, although slow variations on timescales of several hours could be observed in the light curves, we note a lack of any significant signal attributed to rotation modulation.

3.2 UV Temporal analysis

In the following, we examine the UV emission for three stars with FUV observations and two stars with NUV observations. UV fluxes were calculated by multiplying the unit conversion factor to the measured counts per second for each filter (Tandon et al., 2020). The measured FUV and NUV fluxes for BO Mic and GJ 3331 are listed in Table 3.

- **BO Mic:** In Figure 5, we plot the combined orbit FUV light curve for BO Mic observed with F148W filter and binned to 50s. We observe the large flare-like event (event 1) in both X-rays and FUV. The flux increases from 0.2×10^{-14} to $1.02 \times 10^{-14} \text{ ergs cm}^{-2} \text{ s}^{-1} \text{ Å}^{-1}$ in FUV.

- **GJ 3331:** In Figure 6, we plot the combined orbit light curves for NUV band observed with N279N filter (left panel) and FUV with F148W filter (right panels). The average NUV and FUV fluxes is 2.5×10^{-15} and $1.1 \times 10^{-14} \text{ ergs cm}^{-2} \text{ s}^{-1} \text{ Å}^{-1}$, respectively. Although the light curve shows small scale modulation we were unable to obtain any significant periodicities associated with the modulation.

- **DG CVn:** In Figure 7, we plot the combined orbit NUV light curve observed with N242W filter (top panel) and FUV light curve (bottom panel) observed F148W filter. Both the light curves are binned to 15s. A flare-like event observed in X-ray (Event 2 in Figure 4) which occurred around MJD~2457884.79 was also covered by both the UV filters. During this event the flux increased from the quiescent value of $\sim 0.13 \times 10^{-14}$ to $\sim 0.41 \times 10^{-14} \text{ ergs cm}^{-2} \text{ s}^{-1} \text{ Å}^{-1}$ in NUV and FUV bands. The flux changes by a factor of 3.2, however, we do not resolve the rise and decay phase of the event. Although we observe X-ray excess in the SXT light curve (DG CVn Event 3 Fig 4), we believe the flare rise and decay information is lost due to Earth block in UV and X-rays, respectively.

3.3 X-ray Spectral Analysis

Spectral analysis was carried out with XSPEC version 12.9.1. (Arnaud, 1996) distributed with the heasoft package (version 6.20). The spectra were fitted with optically-thin plasma emission models known as Astrophysical Plasma Emission Code (*apec*) as described by Smith et al. (2001) using the atomic database AtomDB version 3.0.7². The spectral data used for fitting were restricted to 0.35-4.5 keV due to uncertainty in the background subtraction above 4.5 keV. The SXT spectra for all our targets are shown plotted in Figure 8 and Figure 9.

To account for the absorption of X-ray photons by interstellar material, a multiplicative absorber model called *Tbabs* was employed. The equivalent Galactic neutral hydrogen column density (N_H) was fixed at a low value of 10^{20} cm^{-2} . The elemental abundance table *aspl* (Asplund et al., 2009) was used in our analysis.

We used the χ^2 minimisation technique to find the best-fit parameters of the plasma emission models. We present the results of our final best fitting model, including the values of the parameters derived, along with their 90% confidence error range in Table 4.. Vari-

²<http://www.atomdb.org>

Table 3. Measured FUV and NUV fluxes

Star name	FUV	NUV
BO Mic (quiet)	2.1 ± 0.4	–
BO Mic (flare)	7.8 ± 0.5	
DG CVn	1.2 ± 0.5	2.0 ± 0.7
GJ 3331	1.1 ± 0.3	2.5 ± 1.1

Note: All errors quoted are with 90% confidence.

Fluxes in 10^{-15} ergs $\text{cm}^2 \text{s}^{-1}$ were calculated using the unit conversion (UC) factor $\times 10^{-15}$, where UC is: 3.09 ± 0.03 for F148W, 0.22 ± 0.001 for N242W, 3.50 ± 0.04 for N279N (Tandon et al., 2020).

ous model combinations were examined to arrive at the best-fitting models, and the corresponding results are provided in Table 4.. We started with assuming a single temperature model *apec* with solar abundances, and then progressed to non-solar abundances before trying additional temperature components and thus converging to the final best-fit models shown in Table 4.. The elemental abundances for all the temperature components were assumed to be the same in each case. We find that two temperature component models with sub-solar abundances lead to acceptable best fits and provide an adequate description of the data for three stars: BO Mic, DG CVn and GJ331. AB Dor, however, required a minimum of three temperature components with sub-solar abundances.

During the quiescence and the flare observed from BO Mic, we carried out a quantitative study of plasma temperatures and global abundance values (Figure 9). The plasma emission measure increases with an increase in the temperature. We also notice that the spectra harden as the temperature increases. Furthermore during the flare, the global elemental abundance increases indicating that fresh chromospheric material is transported into the corona changing the elemental abundance temporarily.

4. Discussion and Conclusion

In this work, we have analysed X-ray and far-UV data from *AstroSat* observations of four ultra-fast rotating active stars AB Dor, BO Mic, DG CVn and GJ 3331. These observations provide a valuable insight into X-ray and UV emission of these stars, allowing us to investigate their outer atmospheric properties and activity levels.

1. AB Dor: We found the coronal parameters remained consistent between the two epochs. The spectral analysis revealed a three-temperature

model with temperatures between 0.2-1.0 keV (3-12 MK). In (Lalitha et al., 2013), a fixed four-temperature VAPEC model with KT values of 0.3, 0.6, 1.2, and 2.4 was used, resulting in emission measures ranging from 1.43 to $4.59 \times 10^{52} \text{ cm}^{-3}$. However, due to lower SNR in our data, we employed a three-temperature APEC model instead, allowing the models to vary freely while keeping the abundance fixed across components. The derived temperatures were in the range of 0.25-3.6 keV, with emission measures spanning from 2.2 to $6.4 \times 10^{52} \text{ cm}^{-3}$. Importantly, the measured emission measures from our new work are consistent with those reported in the previous study by (Lalitha et al., 2013). The soft X-ray flux obtained for AB Dor during the two epochs are consistent with the X-ray activity cycle predicted for AB Dor (Lalitha & Schmitt 2013), indicating that the star is heading towards activity maxima. The observed X-ray and FUV fluxes of AB Dor indicate significant activity, with the FUV flux being the brightest among the stars in our study. The archival GALEX FUV flux of AB Dor is $1.3 \times 10^{-14} \text{ ergs s}^{-1} \text{ cm}^{-2} \text{ \AA}^{-1}$, the highest amongst the sample studied in this paper.

2. BO Mic: During our ~ 42 ks exposure, which spans approximately 250 ks, we observed two flares occurring within a few hours, while the remaining light curve showed no major X-ray flux enhancements. During the same time interval, the UV light curve also showed a larger variation in the flux, coinciding with the X-ray events. The X-ray data allowed us to determine the global coronal abundances, temperatures, and emission measures during the different flaring and quiescent states. The observed X-ray luminosity of BO Mic increases from a quiescent value of $\log L_X \sim 29.83$ to 30.72 during the flare. The quiescent luminosity of BO Mic is consistent with the earlier finding of $\log L_X \sim 29.94$ Singh et al. (1999). Furthermore, Makarov (2003) found $\log L_X \sim 31.06$ an order of magnitude higher than our estimate however indicating the excess X-ray might be due to a flaring event similar to our observations. The quiescent FUV fluxes of BO Mic are $2.1 \pm 0.4 \times 10^{-15} \text{ ergs s}^{-1} \text{ cm}^{-2} \text{ \AA}^{-1}$, consistent with GALEX FUV fluxes of $1.7 \times 10^{-15} \text{ ergs s}^{-1} \text{ cm}^{-2} \text{ \AA}^{-1}$.
3. DG CVn: We observed two large flare-like events in the SXT light curves; however, poor signal-to-noise ratio prevented us from carrying out detailed temporal-spectral analysis during quiescent and flaring states. The X-ray data

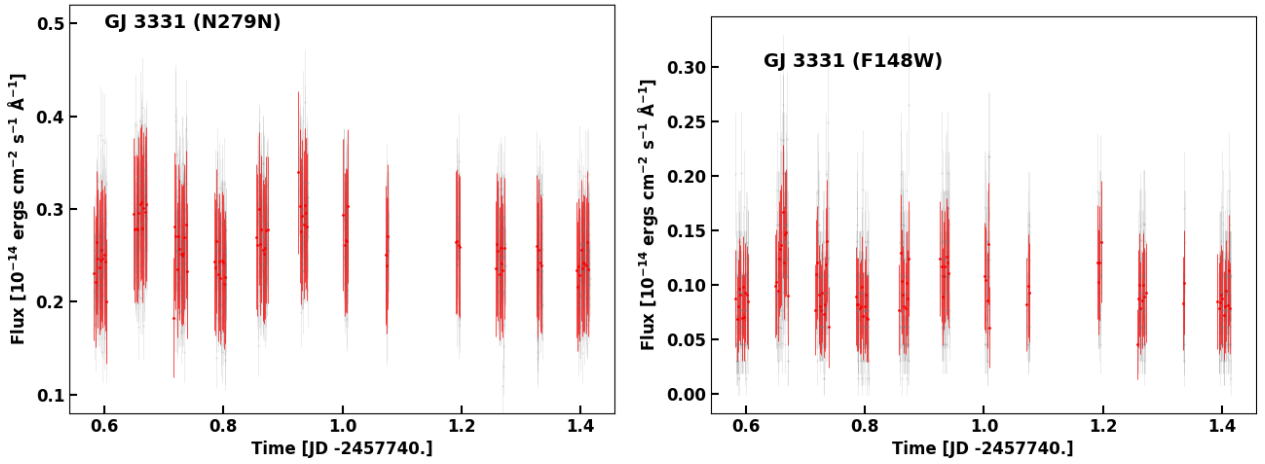


Figure 6. Combined orbits light curves in NUV (left panel) and FUV (right panel) for GJ 3331. The bin widths used are 15s and 20s for NUV and FUV, respectively. For better visualisation of the variability we over plot a moving average light curve in red.

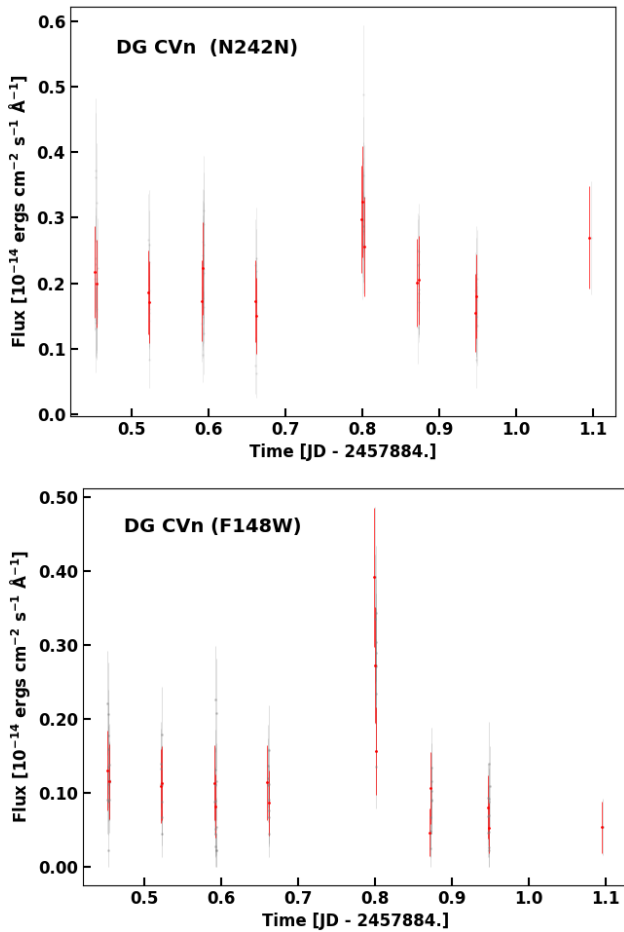


Figure 7. Combined orbits light curve in NUV (top panel) and FUV (bottom panel) for DG CVn binned to 15s. A flare-like event at JD~2457884.079 (see Fig 4).

allowed us to estimate coronal temperatures of 3 MK and 35 MK, consistent with previous findings during the quiescent state of DG CVn Osten et al. (2007). Although visual inspection of DG CVn's FUV and NUV light curves indicated 5-10% modulation in the observed flux with rotation, we did not detect any significant periodicity in our data. The GALEX NUV flux is 1.2×10^{-15} ergs $s^{-1} cm^{-2} \text{Å}^{-1}$, consistent with our measured flux.

4. GJ 3331: The coronal X-ray luminosity measured during our observations is 3.4×10^{29} ergs s^{-1} consistent with the value reported by Voges et al. (1999). The best fit model is a two-temperature *apec* model with sub-solar abundances for all the elements. The best fit temperatures are $0.44^{+0.27}_{-0.13}$ keV and $1.0^{+0.08}_{-0.06}$ keV and the elemental abundances are 0.22 times solar for both the components (See Table 4). The GALEX NUV and FUV are 4.2×10^{-15} and 1.8×10^{-15} ergs $s^{-1} cm^{-2} \text{Å}^{-1}$, respectively. Our measured FUV and NUV fluxes with UVIT are lower than the GALEX fluxes. GJ 3331 has a close companion (GJ 3332) which is not very well resolved in GALEX since the effective aperture of Galex FUV is about twice of UVIT. Hence the GALEX FUV fluxes are significantly higher than our measured fluxes. Consequently, this star has among the highest values of X-ray luminosity to FUV luminosity ratio, indicating high coronal activity for a relatively slow rotator unless the rotation period is indeed as short as 0.34d instead of 9.8d.

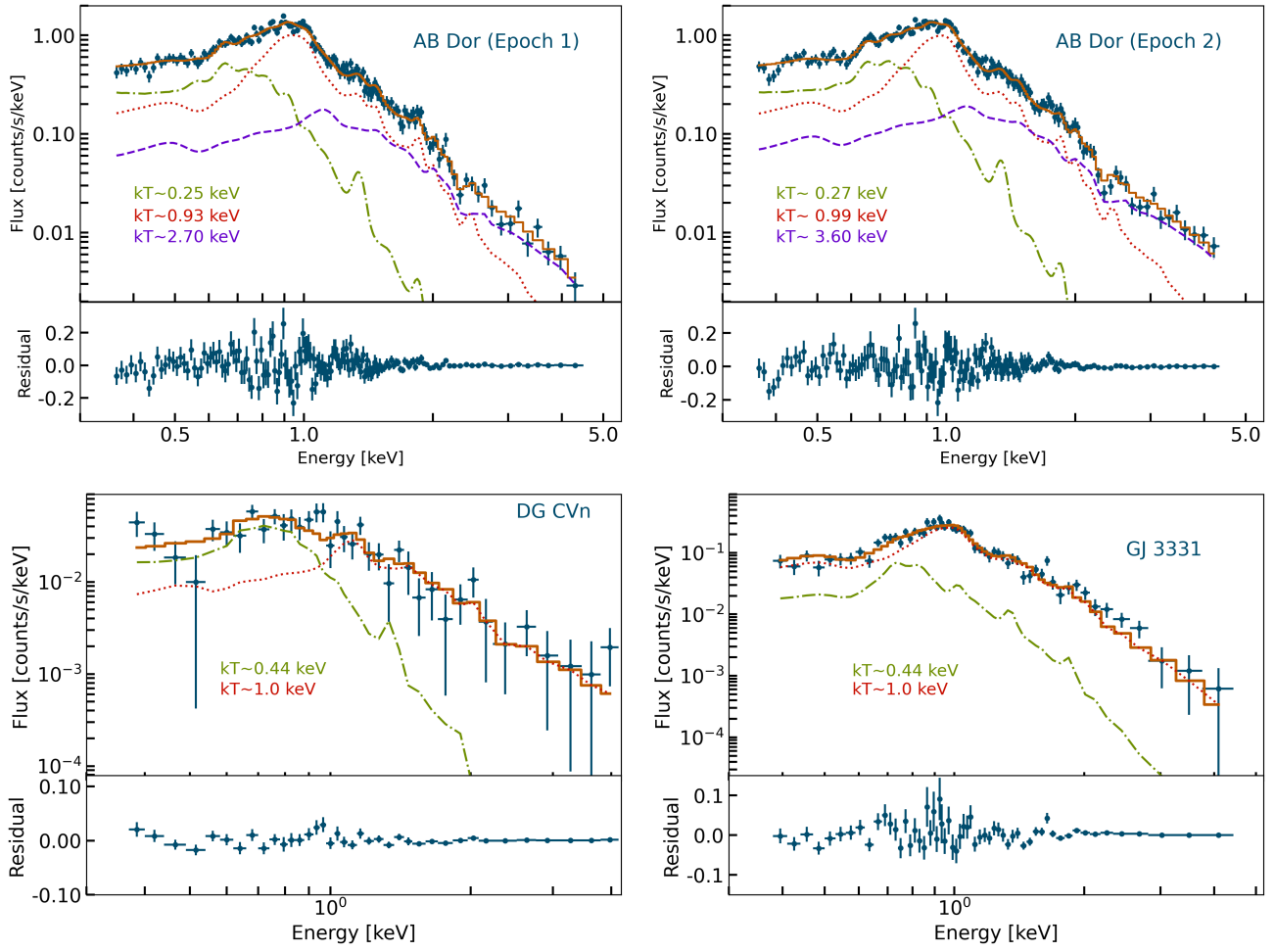


Figure 8. X-ray spectra of AB Dor (two epochs), DG CVn and GJ 3331 along with the best-fit models as observed with *AstroSat* SXT.

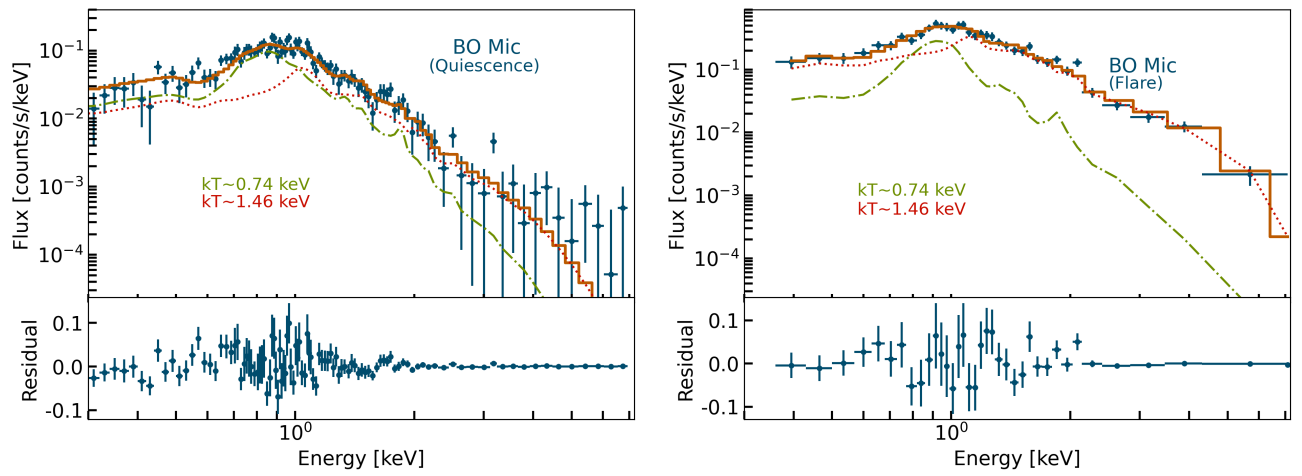


Figure 9. X-ray Spectra of BO Mic and best-fit models as observed with *AstroSat* SXT during the quiescent state (left) and flaring state (right).

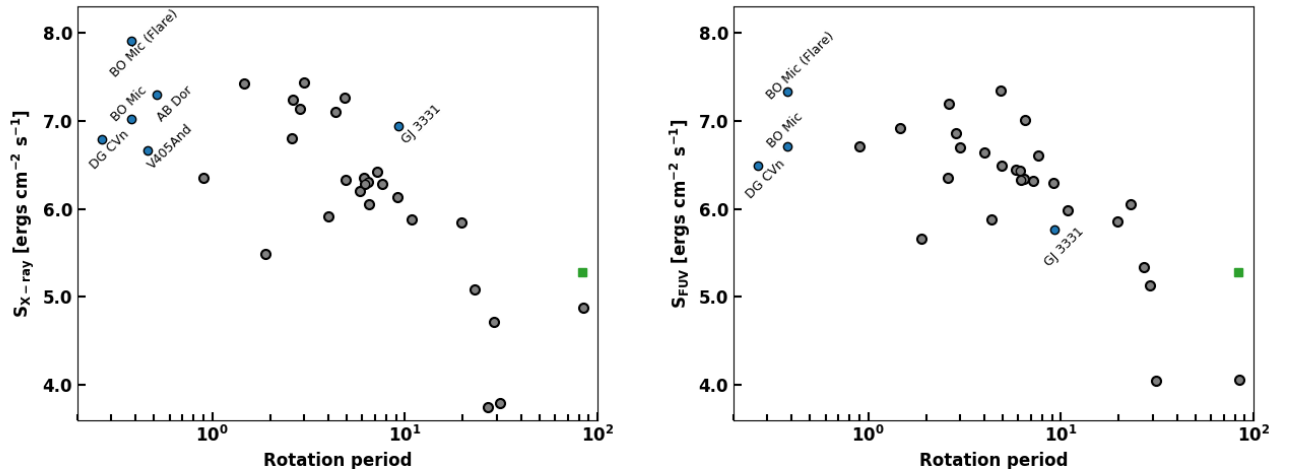


Figure 10. The soft X-ray (left panel) and FUV (right panel) surface fluxes are plotted as a function of the rotation period. The stars studied in this work are depicted as filled circles and open circles depict the stars from (France et al., 2018). Represented as green square is Proxima Centauri observed previously with *AstroSat* (Lalitha et al., 2020) and HST (Youngblood et al., 2017).

Having investigated the individual stars, we compared their X-ray and FUV fluxes with a set of well-studied, non-planet hosting stars from France et al. (2018). These comparison stars encompass a range of spectral types, including F, G, K, and M Dwarfs, and exhibit rotation periods spanning from 0.9 to 100 days. Importantly, both X-ray and UV fluxes have been measured for these stars, making them suitable for our comparative analysis. The X-ray fluxes of these well-studied targets are obtained using ROSAT Position Sensitive Proportional Counters (PSPC) source catalogue Voges et al. (1999). Using XSPEC version 12.9.1 and WebPIMMS v4.11, we convert the flux from canonical ROSAT energy band 0.1-2.4 keV to 0.3-2.0 keV.

In Figure 10 (left panel), the observed X-ray surface flux (0.3-2 keV) of our four targets (filled circles) are compared with the fluxes of the reference targets (open circles and square). To ensure comparability between stars of different sizes, we estimated the surface X-ray fluxes by applying a dilution factor $(\frac{d}{R_\star})^2$ to the observed X-ray flux. The radius values needed to calculate the dilution factor were obtained from France et al. (2018). Note this plot also includes V405 And, yet another ultrafast rotator and a short period RS CVn type binary, observed by *AstroSat*. A detailed analysis of this target will be presented in Pathak et al. (in preparation).

In Figure 10 (right panel), we present the FUV surface flux of BO Mic, DG CVn and GJ 3331 and the comparison stars from France et al. (2018). To compare these FUV fluxes with *AstroSat*'s UVIT F148W, we used the Si IV emission line fluxes (λ 1393.75 Å,

λ 1402.76 Å) observed with HST-STIS France et al. (2018) as a proxy. Similar to the X-ray analysis, we calculated surface FUV fluxes (SFUV) by multiplying the observed FUV flux with the observed bandwidth and the dilution factor of $(\frac{d}{R_\star})^2$.

Overall, the measured surface fluxes at X-ray and FUV wavelengths exhibit a consistent trend, aligning with earlier findings by Stelzer et al. (2013). Both FUV and X-rays demonstrates a slight trend towards the saturation. Note that there is a scarcity of targets with measured FUV and X-ray fluxes for stars with rotation periods < 1 day. Continued observations of ultra-fast rotators in both UV and X-ray wavelengths with *AstroSat*, will enable further insight of these trends associated with the observed surface flux of stars with rotation periods < 1 day. Our current observations provide a foundational basis for conducting comprehensive systematic studies of ultra-fast rotators using multi-wavelength capabilities of *AstroSat*, and from all-sky survey data that would soon become available from *eRosita*.

Table 4. Spectral parameters for the best fit model for the stars observed with the SXT

Star Name	Spectral Model	Parameters kT ₁ keV	Z	EM ₁ 10 ⁵¹ cm ⁻³	kT ₂ keV	EM ₂ 10 ⁵¹ cm ⁻³	kT ₃ keV	EM ₃ 10 ⁵¹ cm ⁻³	χ^2_v/dof	Flux (Soft)	Flux (Hard)
AB Dor (2016 Jan 15-16)	tbabs*(apec+apec+apec)	0.25 ^{+0.013} _{-0.011}	0.36 ^{+0.10} _{-0.08}	62.1	0.93 ^{+0.03} _{-0.03}	45.6	2.7 ^{+1.2} _{-0.5}	22.3	1.16/151	4.3	0.7
AB Dor (2016 Jan 31-Feb 1)	tbabs*(apec+apec+apec)	0.27 ^{+0.015} _{-0.012}	0.35 ^{+0.10} _{-0.08}	64.3	0.99 ^{+0.03} _{-0.03}	47.2	3.6 ^{+1.9} _{-0.8}	26.8	1.05/156	4.5	1.0
BO Mic (Quiescence)	tbabs*(apec+apec)	0.74 ^{+0.06} _{-0.17}	0.27 ^{+0.14} _{-0.10}	2.1	1.46 ^{+0.38} _{-0.31}	1.9	-	-	1.04/101	0.22	0.09
BO Mic (Flare)	tbabs*(apec+apec)	0.96 ^{+0.10} _{-0.11}	0.50 ^{+0.54} _{-0.28}	4.1	3.6 ^{+1.6} _{-0.8}	15.0	-	-	1.21/32	1.71	1.23
DG CVn	tbabs*(apec+apec)	0.27 ^{+0.04} _{-0.03}	1.0	2.71	2.83 ^{+2.8} _{-1.0}	3.60	-	-	1.04/34	0.20	0.07
GJ 3331	tbabs*(apec+apec)	0.44 ^{+0.27} _{-0.13}	0.22 ^{+0.07} _{-0.05}	9.84	1.0 ^{+0.08} _{-0.06}	31.7	-	-	1.44/55	0.76	0.07

Notes: All errors quoted are with 90% confidence. N_H in tbabs is kept fixed at 10^{20} cm⁻² for all spectral models. Abundance, Z, is relative to solar values for all the elements in apec models. EM₁, EM₂ and EM₃ are the emission measures corresponding to temperature components kT₁, kT₂ and kT₃ respectively. Fluxes are in units of 10⁻¹¹ ergs cm⁻² s⁻¹ and are quoted for energy bands of 0.3–2.0 keV (Soft) and 2–6 keV (Hard).

Acknowledgements

This publication uses the data from the *AstroSat* mission of the Indian Space Research Organisation (ISRO). These sources were observed as part of both the SXT guaranteed time program and AO. In particular, the data used were observed from the Soft X-ray Telescope (SXT) developed at TIFR, Mumbai. We thank the SXT and UVIT payload operation centre for verifying, and releasing the data via the ISSDC data archive and providing the necessary software tools. This work has also made use of data from the European Space Agency (ESA) mission *Gaia*³, processed by the *Gaia* Data Processing and Analysis Consortium (DPAC⁴). Funding for the DPAC has been provided by national institutions, in particular, the institutions participating in the *Gaia* Multilateral Agreement. The work has also made use of software, and/or web tools obtained from NASA's High Energy Astrophysics Science Archive Research Center (HEASARC), a service of the Goddard Space Flight Center and the Smithsonian Astrophysical Observatory. K. P. Singh thanks the Indian National Science Academy for support under the INSA Senior Scientist Programme.

³<https://www.cosmos.esa.int/gaia>

⁴<https://www.cosmos.esa.int/web/gaia/dpac/consortium>

Table 5. Best fit spectral parameters for all the models used for arriving at the best model given in Table 4.

Star Name	Spectral Model	Parameters			kT ₂ keV	EM ₂ 10 ⁵¹ cm ⁻³	kT ₃ keV	EM ₃ 10 ⁵¹ cm ⁻³	χ^2_v/dof	Flux (Soft)	Flux (Hard)
		kT ₁ keV	Z	EM ₁ 10 ⁵¹ cm ⁻³							
AB Dor (2016 Jan 15-16)	tbabs*apec	0.85	1.0	31.2	-	-			13.9/156		
	tbabs*apec	0.82	0.09	162.0	-	-			2.97/155		
	tbabs*(apec+apec)	0.75	1.0	22.0	2.35	29.0			7.2/154		
	tbabs*(apec+apec)	0.28 ^{+0.02} _{-0.02}	0.16 ^{+0.02} _{-0.02}	87.0	0.97 ^{+0.02} _{-0.03}	97.0			1.72/153	4.4	0.35
	tbabs*(apec+apec+apec)	0.24 ^{+0.01} _{-0.01}	1.0	30.0	0.93 ^{+0.03} _{-0.03}	18.0	2.9 ^{+0.4} _{-0.3}	24.0	1.40/152	4.3	0.85
AB Dor (2016 Jan 31-Feb 1)	tbabs*apec	0.89	1.0	32.2	-	-			16.1/161		
	tbabs*apec	0.85	0.08	178.0	-	-			23.04/160		
	tbabs*(apec+apec)	0.28	1.0	36.0	1.28	33.0			5.2/159		
	tbabs*(apec+apec)	0.31 ^{+0.03} _{-0.02}	0.15 ^{+0.02} _{-0.02}	87.0	1.04 ^{+0.02} _{-0.03}	105			1.93/158	4.6	0.44
	tbabs*(apec+apec+apec)	0.25 ^{+0.01} _{-0.01}	1.0	30.0	0.98 ^{+0.03} _{-0.03}	17.6	3.4 ^{+0.5} _{-0.4}	31.0	1.28/157	5.2	1.2
BO Mic Quiescence	tbabs*apec	0.95	1.0	1.24	-	-			2.67/104		
	tbabs*apec	0.93±0.04	0.13±0.03	5.2	-	-			1.21/103	0.37	0.04
	tbabs*(apec+apec)	0.76±0.04	1.0	0.8	2.1 ^{+0.7} _{-0.3}	1.4			1.22/102	0.33	0.09
	tbabs*(apec+apec)	0.74 ^{+0.06} _{-0.17}	0.27 ^{+0.14} _{-0.10}	2.1	1.46 ^{+0.38} _{-0.31}	1.9			1.04/101	0.22	0.09
BO Mic Flare	tbabs*apec	1.06	1.0	6.4	-	-			10.97/35		
	tbabs*apec	1.66	0.14	26.4	-	-			2.3/34		
	tbabs*(apec+apec)	0.92±0.09	1.0	2.2	3.9 ^{+1.1} _{-0.7}	13.7			1.24/33	1.66	1.39
	tbabs*(apec+apec)	0.96 ^{+0.10} _{-0.11}	0.50 ^{+0.54} _{-0.28}	4.1	3.6 ^{+1.6} _{-0.8}	15.0			1.21/32	1.71	1.23
DG CVn	tbabs*apec	0.33	1.0	3.2	-	-			3.19/36		
	tbabs*apec	0.74 ^{+0.12} _{-0.12}	0.03 ^{+0.04} _{-0.02}	15.24	-	-			1.24/35	0.20	0.013
	tbabs*(apec+apec)	0.27 ^{+0.04} _{-0.03}	1.0	2.71	2.83 ^{+2.8} _{-1.0}	3.60			1.04/34	0.20	0.07
GJ 3331	tbabs*apec	0.93	1.0	11.4	-	-			3.68/58		
	tbabs*apec	0.91 ^{+0.04} _{-0.03}	0.16 ^{+0.04} _{-0.03}	43.0	-	-			1.55/57	0.75	0.074
	tbabs*(apec+apec)	0.84	1.0	8.3	2.4	9.8			2.02/56	0.66	0.16

Note: All errors quoted are with 90% confidence. N_H in tbabs is kept fixed at 10^{20} cm⁻² for all spectral models. Abundance, Z, is relative to solar values for all the elements in apec model; EM₁, EM₂ and EM₃ are the emission measures corresponding to temperature components kT₁, kT₂ and kT₃ respectively; Fluxes are in units of 10⁻¹¹ ergs cm⁻² s⁻¹ and are quoted for energy bands of 0.3–2.0 keV (Soft) and 2–6 keV (Hard).

References

- Anders G. J., Jeffries R. D., Kellett B. J., Coates D. W., 1993, *MNRAS*, 265, 941
- Arnaud K. A., 1996, in Jacoby G. H., Barnes J., eds, *ASP Conf. Ser. 101: Astronomical Data Analysis Software and Systems V*. pp 17–+
- Asplund M., Grevesse N., Sauval A. J., Scott P., 2009, *ARA&A*, 47, 481
- Azulay R., et al., 2015, *A&A*, 578, A16
- Bromage G. E., Kellett B. J., Jeffries R. D., Innis J. L., Matthews L., Anders G. J., Coates D. W., 1992, in Giampapa M. S., Bookbinder J. A., eds, *Astronomical Society of the Pacific Conference Series Vol. 26, Cool Stars, Stellar Systems, and the Sun*. p. 80
- Clark D. H., Stephenson F. R., 1978, *QJRAS*, 19, 387
- Collier Cameron A., Donati J. F., 2002, *MNRAS*, 329, L23
- Cutispoto G., Kurster M., Pagano I., Rodono M., 1997, *Information Bulletin on Variable Stars*, 4419
- Cutispoto G., Pastori L., Pasquini L., de Medeiros J. R., Tagliaferri G., Andersen J., 2002, *A&A*, 384, 491
- Delfosse X., Forveille T., Perrier C., Mayor M., 1998, *A&A*, 331, 581
- Drake S., Osten R., Page K. L., Kennea J. A., Oates S. R., Krimm H., Gehrels N., 2014, *The Astronomer's Telegram*, 6121
- Drake J. J., Chung S. M., Kashyap V. L., Garcia-Alvarez D., 2015, *ApJ*, 802, 62
- Dunstone N. J., Barnes J. R., Collier Cameron A., Jardine M., 2006, *MNRAS*, 365, 530
- France K., Arulanantham N., Fossati L., Lanza A. F., Loyd R. O. P., Redfield S., Schneider P. C., 2018, *ApJS*, 239, 16
- Gaia Collaboration et al., 2016, *A&A*, 595, A1
- Gaia Collaboration et al., 2018, *A&A*, 616, A1
- Gaia Collaboration et al., 2021, *A&A*, 650, C3
- García-Alvarez D., Drake J. J., Kashyap V. L., Lin L., Ball B., 2008, *ApJ*, 679, 1509
- Gershberg R. E., Katsova M. M., Lovkaya M. N., Terebizh A. V., Shakhovskaya N. I., 1999, *A&AS*, 139, 555
- Güdel M., 2004, *A&A Rev.*, 12, 71
- Guirado J. C., Marcaide J. M., Martí-Vidal I., Le Bouquin J.-B., Close L. M., Cotton W. D., Montalbán J., 2011, *A&A*, 533, A106
- Hathaway D. H., 2015, *Living Reviews in Solar Physics*, 12, 4
- Helfand D. J., Schnee S., Becker R. H., White R. L., McMahon R. G., 1999, *AJ*, 117, 1568
- Hindman B. W., Jain R., 2022, *ApJ*, 932, 68
- Jao W.-C., Henry T. J., Subasavage J. P., Bean J. L., Costa E., Ianna P. A., Méndez R. A., 2003, *AJ*, 125, 332
- Joseph P., Stalin C. S., Tandon S. N., Ghosh S. K., 2021, *JAA*, 42, 25
- Kiraga M., Stepień K., 2007, *Acta Astron.*, 57, 149
- Kochukhov O., 2021, *A&A Rev.*, 29, 1
- Kürster M., 1994, in Klare G., ed., *Astronomische Gesellschaft Abstract Series Vol. 10, Astronomische Gesellschaft Abstract Series*. p. 22
- Lalitha S., Schmitt J. H. M. M., 2013, *A&A*, 559, A119
- Lalitha S., Fuhrmeister B., Wolter U., Schmitt J. H. M. M., Engels D., Wieringa M. H., 2013, *A&A*, 560, A69
- Lalitha S., Schmitt J. H. M. M., Singh K. P., 2017, *A&A*, 602, A26
- Lalitha S., et al., 2020, *MNRAS*, 498, 3658
- Makarov V. V., 2003, *AJ*, 126, 1996
- Malo L., Artigau É., Doyon R., Lafrenière D., Albert L., Gagné J., 2014, *ApJ*, 788, 81
- Mason B. D., Wycoff G. L., Hartkopf W. I., Douglass G. G., Worley C. E., 2001, *AJ*, 122, 3466
- Messina S., Monard B., Biazzo K., Melo C. H. F., Frasca A., 2014, *A&A*, 570, A19
- Mohanty S., Basri G., 2003, *ApJ*, 583, 451
- Osten R. A., Drake S., Tueller J., Cummings J., Perri M., Moretti A., Covino S., 2007, *ApJ*, 654, 1052
- Osten R. A., et al., 2010, *ApJ*, 721, 785
- Osten R. A., et al., 2016, *ApJ*, 832, 174

- Pallavicini R., Golub L., Rosner R., Vaiana G. S., Ayres T., Linsky J. L., 1981, *ApJ*, 248, 279
- Pounds K. A., et al., 1993, *MNRAS*, 260, 77
- Reiners A., Joshi N., Goldman B., 2012, *AJ*, 143, 93
- Romano P., et al., 2005, in Siegmund O. H. W., ed., *Society of Photo-Optical Instrumentation Engineers (SPIE) Conference Series Vol. 5898, UV, X-Ray, and Gamma-Ray Space Instrumentation for Astronomy XIV*. pp 369–376, doi:10.1117/12.616974
- Singh K. P., Drake S. A., Gotthelf E. V., White N. E., 1999, *ApJ*, 512, 874
- Singh K. P., et al., 2014, in *Space Telescopes and Instrumentation 2014: Ultraviolet to Gamma Ray*. p. 91441S, doi:10.1117/12.2062667
- Singh K. P., et al., 2016, in den Herder J.-W. A., Takahashi T., Bautz M., eds, *Society of Photo-Optical Instrumentation Engineers (SPIE) Conference Series Vol. 9905, Space Telescopes and Instrumentation 2016: Ultraviolet to Gamma Ray*. p. 99051E, doi:10.1117/12.2235309
- Singh K. P., et al., 2017, *JAA*, 38, 29
- Smith R. K., Brickhouse N. S., Liedahl D. A., Raymond J. C., 2001, *ApJL*, 556, L91
- Stelzer B., Marino A., Micela G., López-Santiago J., Liefke C., 2013, *MNRAS*, 431, 2063
- Sylwester J., Lemen J. R., Mewe R., 1984, *Nature*, 310, 665
- Tandon S. N., et al., 2017, *JAA*, 38, 28
- Tandon S. N., et al., 2020, *AJ*, 159, 158
- Toriumi S., Airapetian V. S., 2022, *ApJ*, 927, 179
- Usoskin I. G., 2017, *Living Reviews in Solar Physics*, 14, 3
- Voges W., et al., 1999, *A&A*, 349, 389
- Wittmann A. D., Xu Z. T., 1987, *A&AS*, 70, 83
- Wolter U., Schmitt J. H. M. M., van Wyk F., 2005, *A&A*, 435, 261
- Wolter U., Robrate J., Schmitt J. H. M. M., Ness J. U., 2008, *A&A*, 478, L11
- Youngblood A., et al., 2017, *ApJ*, 843, 31